

# Full-Spectrum Spectral Imaging System Analytical Model

John P. Kerekes, *Senior Member, IEEE*, and Jerrold E. Baum

**Abstract**—In support of hyperspectral sensor system design and parameter tradeoff investigations, an analytical end-to-end remote sensing system performance forecasting model has been extended to cover the visible through longwave infrared portion of the optical spectrum (0.4–14  $\mu\text{m}$ ). The model uses statistical descriptions of surface spectral reflectances/emissivities and temperature variations in a scene and propagates them through the effects of the atmosphere, the sensor, and processing transformations. A resultant system performance metric is then calculated based on these propagated statistics. This paper presents theory for the analytical transformation of surface statistics to at-sensor spectral radiance statistics for a downward-looking hyperspectral sensor observing both reflected sunlight and thermally emitted radiation. Comparisons of the model predictions with measurements from an airborne hyperspectral sensor are presented. Example parameter trades are included to show the utility of the model for applications in sensor design and operation.

**Index Terms**—Full-spectrum modeling, hyperspectral imaging, midwave infrared (MWIR), multispectral imaging, remote sensing system modeling, thermal infrared.

## I. INTRODUCTION

**H**YPERSPECTRAL imaging (HSI) systems operating in the reflective solar portion of the optical spectrum (0.4–2.5  $\mu\text{m}$ ) have demonstrated utility in a variety of applications ranging from environmental monitoring [1] to subpixel object detection [2]. The limiting requirement of solar illumination for these systems has motivated development of thermal infrared hyperspectral systems with the hope of achieving similar utility, but with a day/night capability. Also, because some materials have stronger and more distinct spectral features in the midwave infrared (MWIR) and longwave infrared (LWIR), MWIR/LWIR systems offer the possibility of additional applications for hyperspectral sensing.

Previously, an end-to-end reflective solar hyperspectral remote sensing system model was developed using an analytical framework [3] that built on earlier work [4]. This model, known as forecasting and analysis of spectroradiometric system performance (FASSP), has been used for sensitivity studies and requirements analysis for systems operating in the reflective solar portion of the spectrum. The work described in this present

Manuscript received March 10, 2004; revised September 15, 2004. This work was sponsored by the Department of the Defense under Contract F19628-00-C-0002. Opinions, interpretations, conclusions, and recommendations are those of the authors and are not necessarily endorsed by the U.S. Government. This work was performed while the first author was with Lincoln Laboratory.

J. P. Kerekes is with the Center for Imaging Science, Rochester Institute of Technology, Rochester, NY 14623 USA (e-mail: kerekes@cis.rit.edu).

J. E. Baum is with the Lincoln Laboratory, Massachusetts Institute of Technology, Lexington, MA 02420 USA.

Digital Object Identifier 10.1109/TGRS.2004.841428

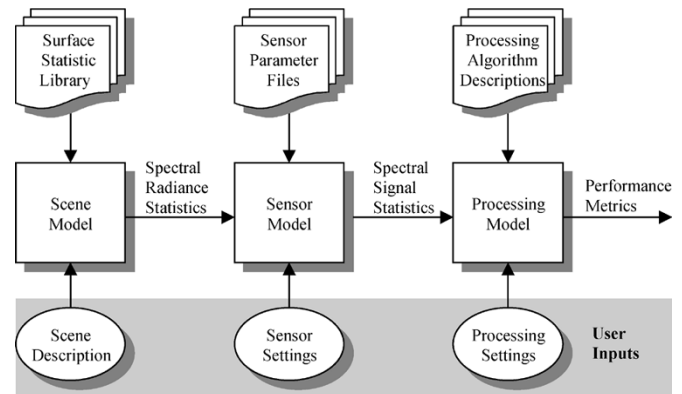


Fig. 1. Block diagram of spectral imaging system analytical model. The diagram shows the flow of the surface statistics from the library through the scene, sensor, and processing models to predict a performance metric.

paper extends the model's capability to analyze systems operating throughout the optical spectrum (0.4–14  $\mu\text{m}$ ).

The following section (Section II) describes the end-to-end model's general approach and applications. Section III presents a description of the model theory developed for a full-spectrum scene. Section IV describes the generic sensor model used in our studies as well as a special case model for the radiometric noise in Fourier transform spectrometers. Section V presents comparisons between model predictions and characteristics of measured airborne thermal infrared hyperspectral data, as well as full-spectrum simulated data. Section VI presents examples of results obtained from analyses conducted with the model. The paper concludes (Section VII) with a summary and discussion of the model's limitations, including areas of ongoing research to overcome these limitations.

## II. ANALYTICAL END-TO-END SYSTEM MODEL

The underlying premises of the model are: 1) that the various surface classes and subclasses of interest can be represented by first- and second-order spectral and temperature statistics and 2) that the effects of various processes in the end-to-end spectral imaging system can be modeled as transformations and functions of those statistics. The end-to-end system includes the scene (illumination, surface, and atmospheric effects), the sensor (spatial, spectral, and radiometric effects), and the processing algorithms (calibration, feature selection, application analysis) that produce a data product. Fig. 1 presents a block diagram of the model and associated supporting data files.

The model is driven by a user-specified input set of system parameters that define the end-to-end scenario, including the scene classes, atmospheric state, sensor characteristics, and processing algorithms. The model operation begins with the surface

spectral (reflectance/emittance) and temperature statistics that are transformed to at-sensor spectral radiance statistics through functions of atmospheric radiative transfer functions. These radiance statistics are then further transformed by linear operations of the sensor including channel spectral response functions and fixed and random sensor errors. The sensor output statistics are then transformed through user-selectable processing functions to result in a performance metric such as spectral characterization accuracy, or a probability of detection versus false alarm curve ( $P_D/P_{FA}$ ). Our previous work [3] described in detail the equations used to propagate the statistics through the end-to-end model to obtain a performance metric for the reflective solar part of the spectrum, while this current work focuses on the extension to the combined reflected and emitted radiance case.

### III. FULL-SPECTRUM SCENE MODEL

The FASSP scene radiance model considers a scene to consist of one or more stochastic background classes and one stochastic target class that may be a linear mixture of target component subclasses. Each background class is defined by the fraction of the scene occupied by that class and a set of statistics. The target is usually considered to be subpixel, or at most, to occupy a single pixel. The statistics for each class or subclass include the mean temperature  $\bar{T}$ , the temperature variance  $\sigma_T^2$ , the mean spectral reflectance  $\bar{\rho}_\lambda$ , and the full-spectral reflectance covariance matrix<sup>1</sup>  $\Sigma_\rho$ . The following sections describe how these surface statistics are transformed into at-sensor radiance statistics.

The model treats all other parameters that affect the at-sensor radiance (e.g., solar illumination angle, visibility, atmospheric water vapor, etc.) as deterministic variables. That is, the user specifies these parameters at the beginning of an analysis. Trade studies can be conducted by the user to investigate how these parameters affect end-to-end system performance by setting up a sequence of runs specifying a set of parameter values for the study.

#### A. At-Sensor Spectral Radiance

The model for the at-sensor spectral radiance has five terms, as shown in (1). The first two terms represent the solar radiance contributions, while the last three describe the thermally emitted radiance components<sup>2</sup>

$$L_{\text{At-Sensor}} = \frac{1}{\pi} [E_S + E_{\text{DS}}] \rho \tau + L_P(\rho_{\text{adj}}) \quad (\text{reflected sunlight}) \\ + L_B(T) [1 - \rho] \tau + \frac{1}{\pi} E_{\text{DT}} \rho \tau \\ + L_U \quad (\text{emitted thermal}) \quad (1)$$

where

- $L_{\text{At-Sensor}}$  spectral radiance received by the downward looking sensor from a given location on the earth's surface;
- $E_S$  solar spectral irradiance incident on surface from direct transmission through atmosphere;

<sup>1</sup>Note: Throughout the paper it is assumed that the surface reflectance  $\rho$  is equal to one minus the emittance  $\varepsilon$  and that the spectral reflectance covariance  $\Sigma_\rho$  is exactly equal to the spectral emittance covariance  $\Sigma_\varepsilon$ .

<sup>2</sup>Note: All radiance calculations are performed in the model as functions of wavelength, but, for clarity in presentation, the subscript  $\lambda$  has been dropped.

- $E_{\text{DS}}$  diffuse atmospherically scattered solar spectral irradiance incident on surface;
- $\rho$  spectral hemispherical reflectance factor for location on surface within sensor instantaneous field of view (IFOV);
- $\tau$  atmospheric transmittance for path from the surface to the sensor;
- $L_P(\rho_{\text{adj}})$  path-scattered solar spectral radiance incident at sensor including the contribution from surface interactions outside the sensor IFOV (adjacency effect);  $\rho_{\text{adj}}$  is the hemispherical reflectance factor for the composite surface outside the sensor IFOV;
- $L_B(T)$  surface-emitted spectral radiance from a black-body at temperature  $T$ ;
- $E_{\text{DT}}$  downwelling atmospheric thermally emitted spectral irradiance incident on surface;
- $L_U$  upwelling atmospheric thermally emitted spectral radiance incident at sensor.

Note that the model does not explicitly account for three-dimensional structure in the surface classes. However, variability resulting from random orientations is modeled through the stochastic representations of the surface reflectances.

#### B. Scalar Radiance Statistics

We begin by describing the full-spectrum scene model for the scalar case of a single wavelength and then extend the results to the vector case of multidimensional statistics.

In our model, the surface reflectance factor  $\rho$  (including the adjacent background  $\rho_{\text{adj}}$ ) and the surface temperature  $T$  are assumed to be random parameters. The spectral reflectance of a given surface class (or subclass) is defined by its mean  $\bar{\rho}$  and standard deviation  $\sigma_\rho$ . The surface temperature  $T$  of a given class is defined by its mean  $\bar{T}$  and standard deviation  $\sigma_T$ . One important assumption is that  $\rho$  and  $T$  are assumed to be statistically independent. This is a reasonable assumption given complex external influences (local radiation environment, wind and solar loading history, etc.) that are specific to a given situation and beyond the scope of our analytical model. All other environmental scene parameters (atmospheric profile, etc.) are assumed to be deterministic with user-specified values.

By combining terms and converting all quantities to radiance, (1) can be written as

$$L_{\text{At-Sensor}} = L_D \rho \tau + L_B(T) [1 - \rho] \tau + L_P(\rho_{\text{adj}}) + L_U \quad (2)$$

where  $L_D$  is the total downwelling (solar + atmospheric thermal) radiance.

The mean value of the at-sensor radiance  $\bar{L}_{\text{AS}}$  is found by taking the expectation of (2) as follows:

$$\bar{L}_{\text{AS}} = E\{L_{\text{At-Sensor}}\} \\ = L_D \bar{\rho} \tau + L_B(\bar{T}) [1 - \bar{\rho}] \tau + L_P(\bar{\rho}_{\text{adj}}) + L_U. \quad (3)$$

Here we have the following:

- $\bar{\rho}$  mean hemispherical reflectance factor;
- $\bar{T}$  mean temperature;
- $\bar{\rho}_{\text{adj}}$  mean hemispherical reflectance factor of adjacent background.

This result follows, since  $\rho$  and  $T$  are independent, and the Planck radiance  $L_B$  is treated as a linear function of temperature near its mean  $\bar{T}$ . Also, the  $\bar{\rho}_{\text{adj}}$  factor is the weighted average of

the surface reflectance of the nearby area and will be discussed later in Section III-D.

The variance of the at-sensor radiance is defined in the usual manner as the expectation of the square of the radiance minus its mean value

$$\sigma_{LAS}^2 = E \{ (L_{AS} - \bar{L}_{AS})^2 \}. \quad (4)$$

The Appendix provides the derivation for the result shown in (5)

$$\sigma_{LAS}^2 = \tau^2 \left[ \sigma_{\rho}^2 \sigma_{LB}^2 + \sigma_{\rho}^2 \bar{L}_B^2 + \sigma_{LB}^2 (1 - \bar{\rho})^2 + \sigma_{\rho}^2 L_D^2 - 2\sigma_{\rho}^2 L_D \bar{L}_B \right] + \sigma_{LP}^2. \quad (5)$$

Here we have the following:

- $\sigma_{\rho}^2$  variance of the surface hemispherical spectral reflectance factor;
- $\sigma_{LB}^2$  variance of the surface radiance emitted by a blackbody at temperature  $\bar{T}$ , calculated as  $(\sigma_T \partial B / \partial T)^2$  for  $T = \bar{T}$ , where  $\sigma_T$  is the surface temperature standard deviation, and  $\partial B / \partial T$  is the derivative of the Planck radiance function;
- $\bar{L}_B$  Planck radiance for a blackbody at temperature  $\bar{T}$ ;
- $\bar{\rho}$  mean hemispherical reflectance factor;
- $L_D$  total downwelling (solar + atmospheric thermal) radiance;
- $\sigma_{LP}^2$  variance of the path-scattered radiance, calculated by scaling the class-averaged variance of nearby surface reflectance  $\sigma_{\rho, \text{adj}}^2$  by the square of the difference between path radiance calculated by moderate resolution transmittance code (MODTRAN) for surface albedo's equal to 0 and 1.

The various radiance and transmittance components are computed using the Air Force Research Laboratory's MODTRAN [5] radiative transfer code or the Planck radiance equation.

### C. Vector Multidimensional Radiance Statistics

The extension of the statistics to the vector case is straightforward. For the elements of the mean vector, one uses (3) separately for each wavelength band. The spectral radiance covariance matrix  $\Sigma_{\text{At-Sensor}}$  is derived in a manner analogous to the scalar radiance variance and is shown below. All matrices are  $K \times K$ , where  $K$  is the number of spectral bands

$$\begin{aligned} \Sigma_{\text{At-Sensor}} = & T \left[ \Lambda_{\sigma_{LB}} \Sigma_{\rho} \Lambda_{\sigma_{LB}} + \Lambda_{\bar{L}_B} \Sigma_{\rho} \Lambda_{\bar{L}_B} \right. \\ & + \Lambda_{1-\bar{\rho}} \Sigma_{L_B} \Lambda_{1-\bar{\rho}} + \Lambda_{L_D} \Sigma_{\rho} \Lambda_{L_D} \\ & \left. - \left( \Lambda_{L_D} \Sigma_{\rho} \Lambda_{\bar{L}_B} + \Lambda_{\bar{L}_B} \Sigma_{\rho} \Lambda_{L_D} \right) \right] T \\ & + (\Lambda_{LP_1} - \Lambda_{LP_0}) \Sigma_{\rho, \text{adj}} (\Lambda_{LP_1} - \Lambda_{LP_0}) \quad (6) \end{aligned}$$

where

- $T$  diagonal matrix of surface-to-sensor atmospheric transmittance;
- $\Lambda_{\sigma_{LB}}$  diagonal matrix of surface-emitted spectral radiance standard deviation with each entry,  $\sigma_{LB} = \sigma_T \partial B / \partial T$  for  $T = \bar{T}$ , where  $\sigma_T$  is the surface temperature standard deviation and  $\partial B / \partial T$  is the derivative of the Planck radiance function;
- $\Sigma_{\rho}$  full-spectral reflectance covariance matrix;
- $\Lambda_{\bar{L}_B}$  diagonal matrix of mean Planck spectral radiance emitted by the surface (assumes blackbody surface) at temperature  $\bar{T}$ ;
- $\Sigma_{L_B}$  spectral covariance of surface-emitted blackbody spectral radiance ( $= \Lambda_{\sigma_L} [1] \Lambda_{\sigma_L}$ , where  $[1]$  is a  $K \times K$  matrix of ones);
- $\Lambda_{1-\bar{\rho}}$  diagonal matrix of  $1 - \bar{\rho}$ —mean surface reflectance;
- $\Lambda_{L_D}$  diagonal matrix of downwelling spectral radiance;
- $\Lambda_{LP_{\alpha}}$  diagonal matrix of path-scattered spectral radiance for a surface albedo of  $\alpha$ .

As before, the various components are computed using the Air Force Research Laboratory's MODTRAN radiative transfer code or the Planck radiance equation.

### D. Multiclass Scene Model

While the above derivation was for a single homogenous class, it can be extended to the multiclass target and background scene model situation. We assume that the object of interest, or target, is composed of  $M$  distinct materials (or subclasses) and the observed radiance from the object is the weighted linear combination of the radiance from each material. Each material  $m$  occupies some area fraction  $a_m$  ( $\sum_{m=1}^M a_m = 1$ ) of the target sensor IFOV, or pixel. The resulting observed spectral radiance is computed as the area weighted sum of terms from (2) as in

$$L_{\text{Target-AS}} = \sum_{m=1}^M L_D a_m \rho_m \tau + \sum_{m=1}^M L_B (T_m) a_m \cdot [1 - \rho_m] \tau + L_p(\rho_{\text{adj}}) + L_U. \quad (7)$$

Note that one of the  $m$  material subclasses may be the "background" material and thus this model supports the subpixel target case.

To compute the composite mean spectral radiance of the target pixel, (7) is used directly by substituting the mean values for  $\rho$ ,  $T$ , and  $\rho_{\text{adj}}$ .

The at-sensor radiance spectral covariance matrix for the composite pixel of interest is computed as in (8), shown at the bottom of the page.

The at-sensor radiance statistics for each of the background class(es) are computed using (6). The composite (all background classes combined together) scene background is represented in a slightly different manner.  $N$  background

$$\begin{aligned} \Sigma_{\text{Target-At-Sensor}} = & T \left[ \sum_{m=1}^M a_m^2 \left\{ \Lambda_{\sigma_{LBm}} \Sigma_{\rho_m} \Lambda_{\sigma_{LBm}} + \Lambda_{\bar{L}_{Bm}} \Sigma_{\rho_m} \Lambda_{\bar{L}_{Bm}} + \Lambda_{1-\bar{\rho}_m} \Sigma_{L_{Bm}} \Lambda_{1-\bar{\rho}_m} + \Lambda_{L_D} \Sigma_{\rho_m} \Lambda_{L_D} \right. \right. \\ & \left. \left. - \left( \Lambda_{L_D} \Sigma_{\rho_m} \Lambda_{\bar{L}_{Bm}} + \Lambda_{\bar{L}_{Bm}} \Sigma_{\rho_m} \Lambda_{L_D} \right) \right\} \right] T + (\Lambda_{LP_1} - \Lambda_{LP_0}) \Sigma_{\rho, \text{adj}} (\Lambda_{LP_1} - \Lambda_{LP_0}) \quad (8) \end{aligned}$$

classes are defined with each occupying  $b_n$  ( $\sum_{n=1}^N b_n = 1$ ) fraction of the total scene. The composite scene average reflectance factor  $\bar{\rho}_{\text{adj}}$  is then computed

$$\bar{\rho}_{\text{adj}} = \sum_{n=1}^N b_n \bar{\rho}_n. \quad (9)$$

This formulation of the adjacency reflectance assumes the scene is of the same scale as the scattering due to atmospheric particles. Studies have shown the scattering of radiance from nearby areas into a sensor's IFOV (adjacency effect) ranges from hundreds of meters to kilometers [6]. This is typically the scale of a scene analyzed with our model.

The composite scene average reflectance background covariance matrix  $\Sigma_{\rho\text{-adj}}$  is computed as shown in (10). This matrix models the usual background covariance estimated from all pixels in a given image. Note that since it is computed by totaling up a weighted sum of reflectance factors from the various background classes in the scene, the composite covariance is a simple linear weighting of the individual covariances  $\Sigma_{\rho n}$ , as opposed to the square of the weighting

$$\Sigma_{\rho\text{-adj}} = \sum_{n=1}^N b_n \Sigma_{\rho n}. \quad (10)$$

#### E. Sources of the Surface Statistics

Because the model is driven by the spectral reflectance statistics, it is important to consider the sources of these statistics. Two, often conflicting, considerations are important in estimating these statistics. First, all samples used should be from a relatively homogenous (single mode) dataset. Second, the largest number of samples possible should be used in estimating the statistics.

In the reflective portion of the spectrum, 0.4–2.5  $\mu\text{m}$ , we have often developed spectral reflectance statistics by transforming airborne HSI data to surface reflectance by applying the empirical line method (ELM). ELM uses in-scene calibration panels of known reflectances to form a linear atmospheric compensation function [7]. Through either supervised selection of homogenous regions, or by unsupervised spectral clustering, large sample sizes of the various surface classes are selected.

In the MWIR and LWIR portion of the spectrum, 2.5–14  $\mu\text{m}$ , the atmospheric compensation techniques are less mature, and to date have limited our ability to develop accurate estimates of the reflectance/emissivity statistics. Also, in this spectral region, the variability of the reflectance/emissivity is small, thus requiring the compensation be performed even more accurately.

As alternative sources of samples for the statistics, one can use laboratory or field measurements made with portable spectrometers and reflectance standards to convert the measurements to reflectance units. In these situations, conditions are often controllable and accurate measurements can be made. Unfortunately, the sample sizes are usually inadequate for accurate estimates, particularly for the spectral covariance matrices. However, this does offer a way of obtaining some reasonable estimates of the statistics.

The other surface input statistics for the model are the mean and variance of the class surface temperature. While estimates of typical mean temperatures are easily obtained,

estimates of the variance across an object or natural area can be problematical, particularly from airborne data because of the above-mentioned immaturity of thermal atmospheric compensation techniques. Here, we have usually fallen back on making reasonable assumptions of expected variability and studied the effect on end-to-end analyses using the temperature variance as a parameter.

Another issue regarding the surface statistics is their relationship with sensor spatial resolution. This effect was studied and included in our previous work [4] and modeled with a functional relationship that included a spatial correlation parameter. Our future work plans include revisiting this issue and augmenting the full-spectrum model appropriately, but for now we assume the model analyses are conducted for sensors with a surface spatial resolution comparable to that of the data used to compile the surface spectral statistics in the library.

#### IV. SENSOR MODEL ENHANCEMENTS

The sensor portion of our end-to-end model describes the effects of an imaging spectrometer on the spectral radiance mean  $\bar{L}$  and covariance  $\Sigma_L$  statistics of a scene. For each target and background class, the input radiance statistics of every spectral channel are modified by electronic gain, radiometric noise sources, and relative calibration error to produce radiance signal statistics  $\bar{S}$  and  $\Sigma_S$ . These signal statistics represent the scene as imaged by the spectrometer. The model described here includes radiometric effects, but not spatial or spectral sources of error.

The mean scene radiance is affected only by a gain parameter. All other noise processes modify the diagonal elements of the spectral covariance matrix. The off-diagonal elements remain unchanged because it is assumed there is no channel-to-channel correlation among the noise sources. If a specific sensor is to be modeled and measurements of noise correlations are available, the model can use these data.

Sensor models have been developed for both a dispersive spectrometer and a Fourier transform spectrometer, the latter being most commonly used for the thermal infrared spectral region. The following provides details on those models.

##### A. Dispersive Spectrometer

The generic dispersive spectrometer model covers separately<sup>3</sup> the VNIR, SWIR, MWIR, and LWIR spectral regions. The model can represent typical hyperspectral sensors, with a few hundred spectral channels, and includes approximations for the spectral response functions and radiometric noise sources.

The radiometric noise processes occur in the detector and in the electronics (see Fig. 2). Noise sources arising from the detector include photon (or shot) noise, excess low-frequency noise (ELFN, significant in a certain type of LWIR sensor, see next paragraph), and thermal noise. The noise processes originating in the electronics include quantization noise, bit errors (in recording or transmitting the data), and noise arising within the electrical components.

All of these sources are treated as independent of the input radiance, except the shot noise and ELFN. This latter type is characteristic of Si:As BIB detectors used in a number of LWIR

<sup>3</sup>Common detector materials do not respond across the entire optical spectrum, so, for each spectral region, most instruments have separate focal planes and noise mechanisms.

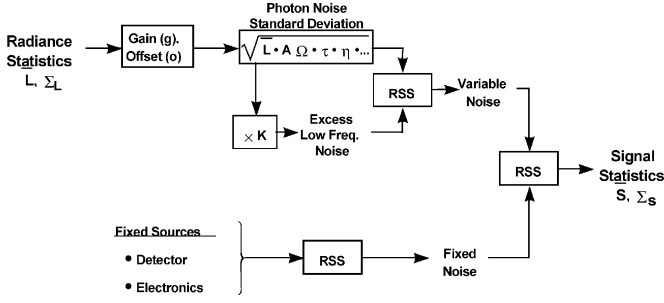


Fig. 2. Block diagram of the dispersive spectrometer radiometric noise model. The excess low-frequency noise term is only applicable for thermal infrared sensors.

sensors [8]. It was recognized in the mid-1980s that, under certain conditions, BIB detectors exhibit a noise level higher than that expected just from shot noise. This “excess” noise occurs at low frequencies and intermediate infrared backgrounds. The excess low-frequency noise does not have  $1/f$  characteristics and is caused by processes internal to the detector. This noise mechanism limits the amount by which the signal-to-noise ratio (SNR) can be improved by co-adding frames because it varies too quickly to be taken out during calibration looks, but also too slowly to have benefits from co-adding frames. ELFN can be modeled as a multiplier, called the “excess noise factor,”  $K$ , of the photon noise. Thus, ELFN increases as photon irradiance increases.

The photon, or shot, noise is a function of, among other variables, the optical transmittance and quantum efficiency. The particular values used in the model for these quantities vary from sensor to sensor and often vary spectrally.

There is some amount of thermal self-radiation from a typical instrument that cannot be shielded from the detector. The noise due to this radiation is combined with other fixed detector noise sources, such as readout noise, into a single value.

### B. Fourier Transform Spectrometer

A Fourier transform spectrometer (FTS) has a number of noise sources that are the same as those found in dispersive spectrometers: photon, detector, and quantization noise, for example. However, because the FTS is a fundamentally different instrument, it also has a number of unique sources of noise, such as mirror velocity errors, sampling errors, and optical jitter. Thus, a new noise model is required, which at this point only includes the dominant noise source of a well-designed instrument: detector noise. This mechanism includes interference caused both by statistical fluctuations in the conversion of photons to electrons (photon noise) and generated by the physical characteristics of the detector material (detector noise).

The initial version of the FTS noise model [9] used in our work specifies the instrument performance in terms of noise equivalent spectral radiance, or  $NEN_\nu$ . This value represents the at-sensor radiance which would produce an output signal equivalent to the instrument noise, at each wavenumber  $\nu$ ; or equivalently, the input radiance that would produce an output SNR of 1. The detector  $NEN_\nu$  is given by

$$NEN_{\nu, \text{det}} = \frac{4L_{\text{OPD}}}{A_o \Omega \tau_{\text{ox}} \eta_s D^*} \sqrt{\frac{A_d}{t}} \frac{\text{watts}}{\text{cm}^2 - \text{sr} - \text{cm}^{-1}} \quad (11)$$

where

- $A_d$  detector area (square centimeters);
  - $A_o$  optical aperture area (square centimeters);
  - $D^*$  detectivity (centimeters  $-\sqrt{\text{Hz}}$  per watt);
  - $L_{\text{OPD}}$  maximum optical path difference (centimeters);
  - $t$  integration time (seconds);
  - $\eta_s$  beamsplitter efficiency;
  - $\Omega$  solid angle field-of-view (steradians);
  - $\tau_{\text{ox}}$  transmittance of optics (excluding beamsplitter).
- $D^*$ , the specific detectivity, is the reciprocal of the noise-

equivalent power, normalized to unit detector area and temporal bandwidth. It is a common figure-of-merit for describing detector performance. Because the interferometer has a finite mirror stroke, the optical path difference between the two arms of the FTS has some maximum value,  $L_{\text{OPD}}$ . This finite value limits the spectral resolution  $\delta\nu$  of the instrument to be

$$\delta\nu = \frac{1}{2L_{\text{OPD}}}. \quad (12)$$

The beamsplitter efficiency  $\eta_s$  has a value between 0 and 1 and is equal to  $4RT$ , where  $R$  and  $T$  are the reflectance and transmission, respectively, of the beamsplitter. For an ideal beamsplitter,  $R = T = 0.5$  and  $\eta_s = 1$ .

## V. VALIDATION

In order to comprehensively validate the full-spectrum scene radiance model we would require a dataset for which accurate estimates of the spectral reflectance and temperature statistics are known for a scene observed by a remote imaging spectrometer covering the full optical spectrum (0.4–14  $\mu\text{m}$ ). However, such a dataset is very difficult to obtain with current instruments and atmospheric compensation algorithms. Not having access to such a validation set, we have chosen to demonstrate the ability of the model to represent the radiance statistics in a manner consistent with observations.

Two experiments are described below. First, in the LWIR spectral region, we compare the mean spectral radiance and radiance variability statistics predicted by the model to observations of airborne spectral data under reasonable assumptions for the surface statistics. The second experiment is a Monte Carlo simulation of a complex scene with a multiclass target to confirm the analytical derivation for the full-spectrum model statistics match the empirical statistics calculated from the simulation.

### A. Airborne LWIR Hyperspectral Data

The model predictions of spectral radiance were compared to airborne LWIR hyperspectral data collected by the dispersive SEBASS [10] instrument on June 27, 1997 at the Department of Energy Atmospheric Radiation Measurements (ARM) site near Lamont, OK. The scene consisted of wheat fields, pasture, and an area where several test panels were deployed.

The measured data and model predictions were compared in two ways. First, for one of the test panels the average at-sensor spectral radiance was computed from the data and compared to the model prediction. Inputs to the model included ground truth emissivity spectra and estimates of the scene parameters (see Table I). Second, over a relatively uniform region of the pasture,

TABLE I  
SCENE CONDITIONS DURING SEBASS OVERFLIGHT JUNE 27, 1997

Parameter	Value
Surface mean temperature	22°C
Surface temperature $\sigma$	0.1°C
Atmospheric model	1976 US Standard
Sensor altitude	2500 ft

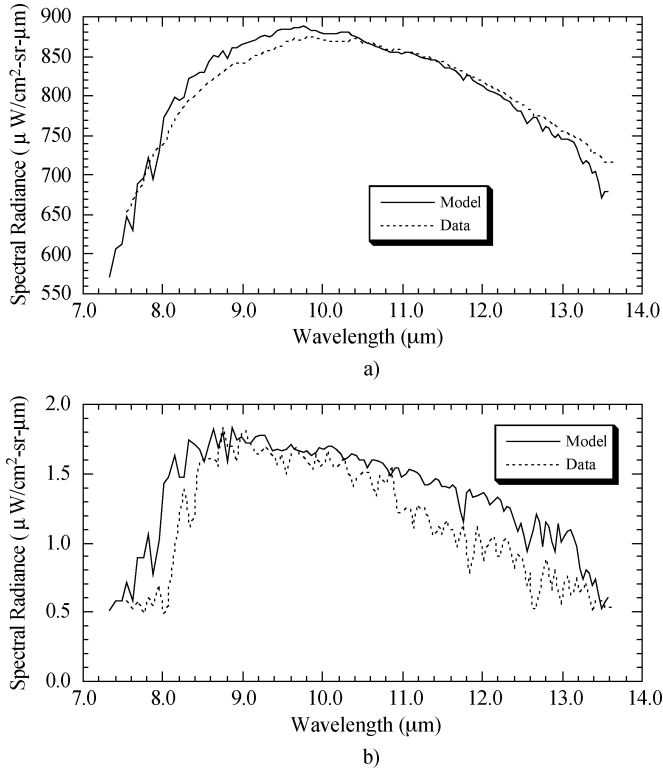


Fig. 3. Comparison of calibrated airborne hyperspectral spectral radiance from the SEBASS sensor with model-predicted spectral radiance using similar conditions. (a) Mean spectral radiance for a test panel. (b) Spectral radiance standard deviation for an area over the pasture.

the variability (standard deviation) of the at-sensor spectral radiance was compared to the variability predicted by the model.

1) *Mean Spectral Radiance Comparison:* The measured mean spectral radiance was calculated by averaging the data from nine pixels centered on the “16%” calibration panel (the 16% percent refers to the visible reflectance of the panel; its LWIR emissivity varied from 0.95 to 0.98). To predict the mean spectral radiance, ground measurements of the panel’s emissivity were input to the model, along with parameters shown in Table I. The comparison is shown in Fig. 3(a). The match between model prediction and data is within 5%. Differences may be explained by errors in the absolute radiometric calibration of the sensor and by differences between the model atmosphere and the real atmosphere at the time of the data collection.

2) *Spectral Radiance Variability Comparisons:* The standard deviation of the calibrated spectral radiance was calculated using one hundred pixels of the measured hyperspectral data over a relatively homogenous area of pasture. Because no accurate emissivity spectra of the pasture were available, a constant greybody mean spectrum with 0.99 emissivity was assumed. The variability of the pasture emissivity was represented with a standard deviation of 0.001.

TABLE II  
SCENE CONDITIONS FOR MULTICLASS MONTE CARLO EXPERIMENT

Parameter	$\lambda_1$	$\lambda_2$	$\lambda_3$
Wavelength ( $\mu\text{m}$ )	0.5	4.0	10.0
Atmospheric transmittance	0.7	0.9	0.8
Downwelling spectral radiance ( $\text{W}/\text{m}^2\text{-}\mu\text{m-sr}$ )	250	1.2	3.8
Upwelling thermal spectral radiance ( $\text{W}/\text{m}^2\text{-}\mu\text{m-sr}$ )	0	0.04	2.0
Upwelling path scattered mean spectral radiance ( $\text{W}/\text{m}^2\text{-}\mu\text{m-sr}$ )	24	0.005	0
Upwelling path scattered standard deviation ( $\text{W}/\text{m}^2\text{-}\mu\text{m-sr}$ )	2	0	0

Fig. 3(b) shows that a comparison of the variability in the sensor data and that predicted by the model have similar overall shapes and magnitudes, but differences of up to 30% to 40% are seen. Many of the same atmospheric features are present in both the measured data and the model prediction, but also there are some shifts seen in their peaks that may be due to spectral calibration errors in the data.

It is important to note that the variability seen in these data come from at least three sources: surface temperature variations, surface emissivity variations, and sensor noise. Examination of the relative values of these three sources in the model predictions shows that the surface temperature variation dominates, with 55% of the total variance and nearly the same shape and magnitude as the total variability. The sensor noise is the next largest contributor with 25% of the variance, and the emissivity standard deviation of 0.001 leads to 20% of the variance in this case. These relative values are consistent with expectations and observed performance of the instrument. While the model seems reasonable in this case, further validation over other sites and materials will be pursued.

## B. Simulated Multiclass Full-Spectrum Data

To test the multiclass full-spectrum model for the propagation of surface statistics to at-sensor radiance statistics, we generated simulated data with specified atmospheric conditions, target and background abundances, and surface reflectance/temperature statistics. We then applied (7) to generate at-sensor radiance samples for a target composed of multiple subclasses. We then estimated the at-sensor statistics of this simulated data and compared it to the statistics predicted by the analytical model.

We selected three wavelengths (one each from the visible, MWIR, and LWIR) to span the spectrum and have a multidimensional case. The atmospheric transmittances and spectral radiances were generated by a sample run of MODTRAN to obtain reasonable numbers for use in the simulation. Table II shows the wavelengths and atmospheric conditions assumed for the simulation experiment.

Table III presents the characteristics of the three surface subclasses that were defined for this experiment. Two hundred thousand samples of simulated at-sensor radiances were generated. A radiance sample from each subclass was calculated and weighted together as in (7) using a random temperature (Gaussian distributed), a random path-scattered radiance (Gaussian distributed), and a random surface reflectance factor (uniformly distributed). The surface reflectance factors were generated to have a full-spectral covariance matrix with the standard deviations and correlation coefficients shown in Table III.

Table IV shows the results for three at-sensor radiance statistics (at each of the three wavelengths) from the Monte Carlo simulation compared to those predicted by the analytical

TABLE III  
SURFACE CLASS STATISTICS FOR MULTICLASS MONTE CARLO EXPERIMENT

Parameter	Class 1	Class 2	Class 3
Fractional abundance	0.3	0.3	0.4
Surface mean temperature (°C)	25	27	30
Surface temperature standard deviation (°C)	0.5	1.0	2.0
Mean reflectance factor			
$\hat{\lambda}_1$	0.05	0.50	0.15
$\hat{\lambda}_2$	0.30	0.40	0.25
$\hat{\lambda}_3$	0.02	0.20	0.05
Reflectance standard deviation			
$\hat{\lambda}_1$	0.02	0.04	0.01
$\hat{\lambda}_2$	0.05	0.03	0.02
$\hat{\lambda}_3$	0.005	0.05	0.005
Reflectance correlation coefficient			
$\hat{\lambda}_{12}$	0.90	0.95	0.80
$\hat{\lambda}_{13}$	0.85	0.75	0.75
$\hat{\lambda}_{23}$	0.95	0.90	0.95

TABLE IV  
COMPARISON BETWEEN SIMULATED EMPIRICAL AND ANALYTICAL MODEL

Parameter	$\hat{\lambda}_1$	$\hat{\lambda}_2$	$\hat{\lambda}_3$
Mean spectral radiance ( $W/m^2\text{-}\mu\text{m}\text{-sr}$ )			
Monte Carlo Simulation	63.4	0.843	9.59
Analytical Model	63.4	0.842	9.59
Standard deviation of spectral radiance ( $W/m^2\text{-}\mu\text{m}\text{-sr}$ )			
Monte Carlo Simulation	3.15	0.020	0.130
Analytical Model	3.16	0.021	0.131
Correlation coefficient ( $\hat{\lambda}_{12}, \hat{\lambda}_{13}, \hat{\lambda}_{23}$ )			
Monte Carlo Simulation	0.254	-0.309	0.610
Analytical Model	0.269	-0.290	0.609

TABLE V  
INPUT CONDITIONS FOR RADIANCE SENSITIVITY ANALYSIS

Parameter	Value
Surface mean reflectance	20%
Surface reflectance $\sigma$	1%
Surface mean temperature	25°C
Surface temperature $\sigma$	1°C
Atmospheric model	Midlatitude Summer
Solar zenith angle	45°
Meteorological range	23 km
Sensor altitude	6 km

model. As can be seen, the analytical model tracks the mean, the spectral variability, and the spectral correlation of the radiances through the illumination and atmospheric effects in a manner quite similar to the Monte Carlo simulation. This result provides confidence in the analytical derivations of the full-spectrum surface to radiance transformations, but does not validate the complete end-to-end model.

## VI. EXAMPLE ANALYSES

As examples of how the model may be used to study system parameters, we present two analyses. The first shows the model's utility in understanding the magnitudes of the various at-sensor radiance components, particularly with regard to how the variability of the surface properties (e.g., temperature, reflectance) propagates to variability of the at-sensor radiance. The second example shows an end-to-end detection analysis and the relative importance of various system parameters.

### A. At-Sensor Radiance Comparisons

Scene conditions were defined as in Table V and input to the model to predict the magnitudes of the various components contributing to the mean and standard deviation of the at-sensor

radiance. Typical variabilities were selected to provide meaningful results. A spectrally flat (across all wavelengths) surface reflectance was chosen so the spectral content of the results depended only on the effects of the atmosphere and Planck radiance functions.

Fig. 4 presents the mean radiance as calculated with MODTRAN. The total at-sensor radiance is plotted along with the four radiance components used in the model: ground-reflected, path-scattered, surface-emitted, and atmospheric-emitted (upwelling) radiances. As expected, the path-scattered and ground-reflected components dominate in the 0.4–2.5  $\mu\text{m}$  spectral region, particularly at the lower wavelength end. In the 3–4- $\mu\text{m}$  region, we see the cross over between the ground reflected and the surface emitted. From 4–14  $\mu\text{m}$ , we see that the surface emitted and atmospheric emitted (upwelling) are comparable, while the ground reflected is an order of magnitude lower.

Fig. 5 plots the standard deviation of the at-sensor radiance and its three components. Each component was calculated by leaving the indicated variability as specified in Table V and setting the other two to zero. Below 3.5  $\mu\text{m}$  the surface reflectance variability dominates, while above 3.5  $\mu\text{m}$  the surface temperature variability dominates. Below 1  $\mu\text{m}$ , the background variability contributes through the adjacency effect, but rapidly falls off at longer wavelengths.

### B. Object Detection Analyses

Detection of a target is enabled by differences (e.g., in temperature or reflectance) between the target and its background and is hindered by variability either in the scene or due to sensor noise. The sensitivity of detection performance was studied as a function of three different system effects as examples of the flexibility of the model. Because our previous work focused on the reflective part of the spectrum, this example addresses the thermal infrared spectral region and includes examples due to surface temperature effects.

An example scenario of detecting a man-made panel in a pasture field was defined. The model scenario uses a matched filter [2] based on the scene background covariance and the mean radiance spectrum from an occurrence of the panel somewhere in the image to detect it elsewhere in the image. The target is assumed to occupy a whole pixel in all cases. Table VI describes system parameters chosen for these sensitivity analyses.

1) *Sensitivity to Target-Background Temperature Differences:* To study the effect of target/background mean temperature differences on detection performance, the background mean temperature was held constant, while the target temperature was varied and detection performance recomputed. Fig. 6 presents the results and shows a clear minimum in detection probability at a target-background temperature difference of 1.4 °C. At this value, the target's higher temperature and a lower emissivity results in a mean spectral radiance nearly equal to that of the background with its lower temperature but higher emissivity. Temperature differences higher or lower than 1.4 °C lead to more contrast, and thus greater detection probabilities.

2) *Sensitivity to Target Temperature Variability:* To study the effect of target temperature variability, its standard deviation was incrementally increased from 0.0 °C to 1.0 °C, while all other parameters were held constant. Fig. 7 presents the results,

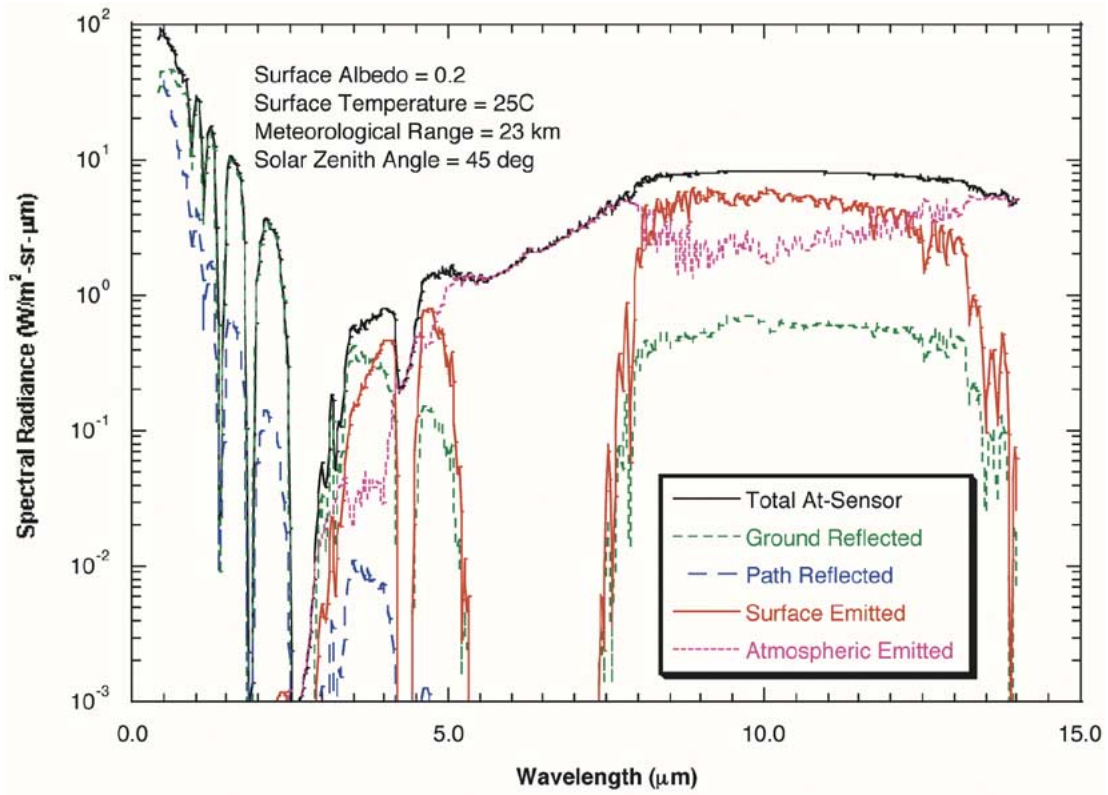


Fig. 4. Example MODTRAN radiance components for nadir-viewing sensor at 6-km altitude.

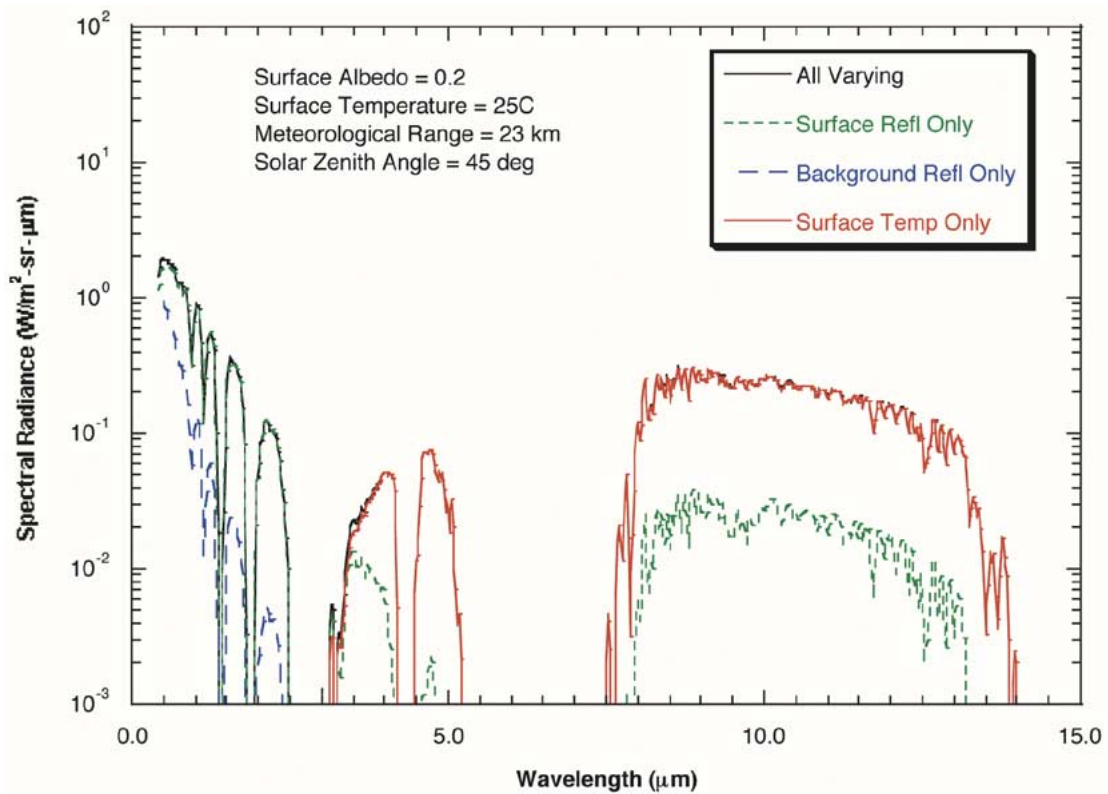


Fig. 5. Example radiance standard deviations due to various components.

TABLE VI  
BASELINE SYSTEM PARAMETERS DEFINED  
FOR DETECTION SENSITIVITY ANALYSES

Parameter	Value
Target	white calibration panel
Target mean emissivity	spectrally varying, 0.95-0.98
Target emissivity $\sigma$	0.0
Target mean temperature	23.75°C
Target temperature $\sigma$	0.1°C
Background	simulated pasture
Background mean emissivity	spectrally constant, 0.99
Background emissivity $\sigma$	0.01
Background mean temperature	22.0°C
Background temperature $\sigma$	0.1°C
Atmospheric model	1976 US Standard
Sensor	SEBASS
Sensor altitude	2500 ft.
Detection algorithm	matched filter
Spectral channels used in filter	38 between 9.0 and 11.0 $\mu\text{m}$
Constant false alarm rate	$10^{-5}$

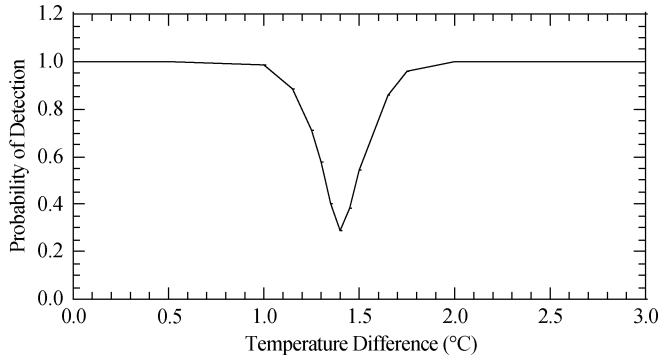


Fig. 6. Detection performance sensitivity to target/background mean temperature difference for system defined in Table VI.

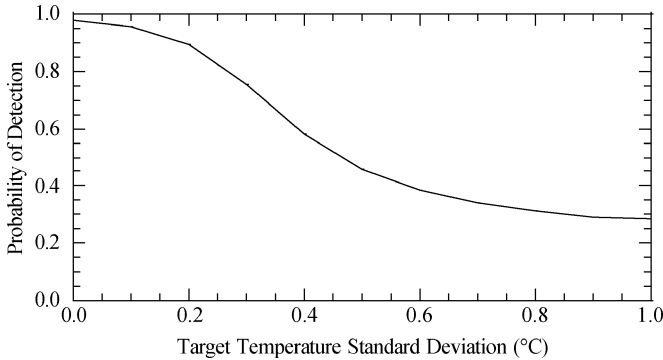


Fig. 7. Detection performance sensitivity to target temperature variability for system defined in Table VI.

which show the expected decrease in detection performance as the target temperature variability increases.

3) *Sensitivity to Sensor Noise:* To study the effect of sensor noise, the standard deviation of the noise was scaled by multiples from 0 to 10, while all other parameters were held constant. Fig. 8 presents the fall-off in detection performance as noise increases. For the given system defined in Table VI, this result shows only modest decreases in detection probability for noise 2 to 3 times the nominal level, but significant effects when the noise is higher by an order of magnitude.

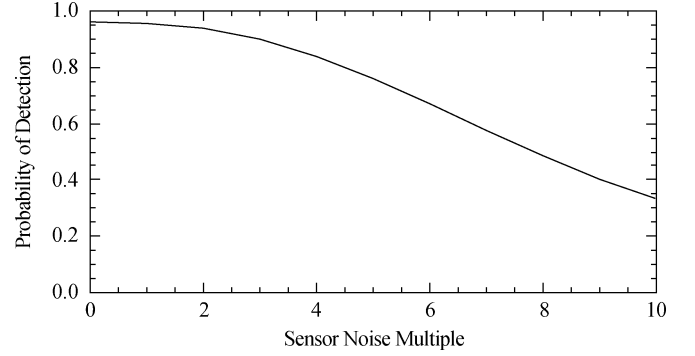


Fig. 8. Detection performance sensitivity to sensor noise scaling for system defined in Table VI.

## VII. SUMMARY AND CONCLUSION

This paper has presented enhancements to an existing hyper-spectral system performance model that extends its operation to span the full surface remote sensing optical spectrum from 0.4–14  $\mu\text{m}$ . The enhancements included combining the surface temperature variability with surface reflectance/emissivity variability in the upwelling radiance calculation. While these enhancements have enabled the full-spectrum modeling of the scene and sensor portions of a remote sensing system, additional work remains to implement model representations of full-spectrum processing algorithms. These include algorithms for atmospheric compensation to retrieve surface reflectance/emissivity and temperature. Also, additional validation efforts should be conducted as appropriate datasets become available.

## APPENDIX

### SPECTRAL RADIANCE VARIANCE

The at-sensor spectral radiance  $L_{\text{At-Sensor}}$  was defined in (2) and is repeated here as

$$L_{\text{AS}} = L_D \rho \tau + L_B(T)[1 - \rho]\tau + L_P(\rho_{\text{adj}}) + L_U. \quad (\text{A1})$$

The random variables in this equation include the surface reflectance  $\rho$ , the surface temperature  $T$ , and the adjacent background surface reflectance  $\rho_{\text{adj}}$ . As noted in the text, these variables are assumed to be statistically independent.

Using standard statistical theory on the variance of linear combinations of variables and the shorthand notation  $L_B(T) = L_B$  and  $L_P(\rho_{\text{adj}}) = L_P$ , we see the variance of  $L_{\text{AS}}$  can be written as

$$\begin{aligned} \text{Var}(L_{\text{AS}}) &= \text{Var}(L_D \rho \tau) + \text{Var}(L_P) + \text{Var}\{L_B(1 - \rho)\tau\} \\ &\quad + 2\text{Cov}\{L_D \rho \tau, L_B(1 - \rho)\tau\} \end{aligned} \quad (\text{A2})$$

$$\begin{aligned} &= \tau^2 L_D^2 \sigma_\rho^2 + \sigma_{L_P}^2 + \tau^2 \text{Var}\{L_B(1 - \rho)\} \\ &\quad + 2\tau^2 \text{Cov}\{L_D \rho \tau, L_B(1 - \rho)\}. \end{aligned} \quad (\text{A3})$$

There are no covariance terms with  $L_P$  and the other terms because  $\rho_{\text{adj}}$  is assumed independent of both  $\rho$  and  $T$ . Only the last two terms in (A3) need expansion.

For two independent variables  $X$  and  $Y$ , the variance of their product is easily seen to be

$$\text{Var}(XY) = \text{Var}(X)\text{Var}(Y) + \text{Var}(X)\{E(Y)\}^2 + \text{Var}(Y)\{E(X)\}^2. \quad (\text{A4})$$

Thus, the variance factor in the third term in (A3) becomes

$$\text{Var}\{L_B(1-\rho)\} = \sigma_{LB}^2\sigma_\rho^2 + \sigma_{LB}^2(1-\bar{\rho})^2 + \sigma_\rho^2\bar{L}_B^2. \quad (\text{A5})$$

Also, the covariance between two random variables is the expectation of their product minus the product of their expectations and the covariance in the fourth term of (A3) becomes

$$\begin{aligned} \text{Cov}\{L_D\rho, L_B(1-\rho)\} &= E\{L_D L_B \rho(1-\rho)\} \\ &\quad - E(L_D\rho)E\{L_B(1-\rho)\} \\ &= L_D E(L_B)E\{\rho(1-\rho)\} \\ &\quad - L_D E(L_B)E(\rho)E(1-\rho) \\ &= L_D \bar{L}_B [E(\rho) - E(\rho^2) - E(\rho) \\ &\quad\quad + E(\rho)^2] \\ &= -L_D \bar{L}_B \sigma_\rho^2. \end{aligned} \quad (\text{A6})$$

Finally, inserting (A5) and (A6) in (A3), we have the result below, which is repeated in the body of the paper as (5)

$$\sigma_{LAS}^2 = \tau^2 \left[ \sigma_\rho^2 \sigma_{LB}^2 + \sigma_\rho^2 \bar{L}_B^2 + \sigma_{LB}^2 (1-\bar{\rho})^2 + \sigma_\rho^2 L_D^2 - 2\sigma_\rho^2 L_D \bar{L}_B \right] + \sigma_{LP}^2. \quad (\text{A7})$$

#### ACKNOWLEDGMENT

The authors acknowledge the support of this work by LT M. Rigo and the Spectral Information Technology Applications Center (SITAC), CAPT F. Garcia (Office of the Deputy Undersecretary of Defense for Science and Technology), and T. Cooley and R. Lockwood (Air Force Research Laboratory Space Vehicles Directorate). The suggestions of the anonymous reviewers were very much appreciated. Also the first author expresses sincere gratitude and appreciation for the guidance of Prof. David Landgrebe during and in the years following his graduate study.

#### REFERENCES

- [1] "Special issue on imaging spectroscopy," *Remote Sens. Environ.*, vol. 65, no. 3, Sep. 1998.
- [2] D. Manolakis, C. Siracusa, and G. Shaw, "Hyperspectral subpixel target detection using the linear mixing model," *IEEE Trans. Geosci. Remote Sens.*, vol. 39, no. 7, pp. 1392–1409, Jul. 2001.
- [3] J. P. Kerekes and J. E. Baum, "Spectral imaging system analytical model for subpixel object detection," *IEEE Trans. Geosci. Remote Sens.*, vol. 40, no. 5, pp. 1088–1101, May 2002.
- [4] J. P. Kerekes and D. A. Landgrebe, "An analytical model of earth-observational remote sensing systems," *IEEE Trans. Syst., Man, Cybern.*, vol. 21, no. 1, pp. 125–133, Jan./Feb. 1991.

- [5] A. Berk, L. S. Bernstein, G. P. Anderson, P. K. Acharya, D. C. Robertson, J. H. Chetwynd, and S. M. Adler-Golden, "MODTRAN cloud and multiple scattering upgrades with application to AVIRIS," *Remote Sens. Environ.*, vol. 65, no. 3, pp. 367–375, Sep. 1998.
- [6] Y. J. Kaufman, "Atmospheric effect on spatial resolution of surface imagery," *Appl. Opt.*, vol. 23, no. 19, pp. 3400–3408, Oct. 1, 1984.
- [7] G. M. Smith and E. J. Milton, "The use of the empirical line method to calibrate remotely sensed data to reflectance," *Int. J. Remote Sens.*, vol. 20, pp. 2653–2662, 1999.
- [8] D. C. Arrington, J. E. Hubbs, M. E. Gramer, and G. A. Dole, "Impact of excess low frequency noise (ELFN) in Si:As impurity band conduction (IBC) focal plane arrays for astronomical applications," in *Proc. SPIE Conf. Infrared Detectors and Focal Plane Arrays V*, vol. 3379, Apr. 1998, pp. 361–370.
- [9] D. R. Hearn, "Fourier Transform Interferometry," Lincoln Lab., MIT, Lexington, MA, Tech. Rep. 1053, 1999.
- [10] J. A. Hackwell, D. W. Warren, R. P. Bongiovi, S. J. Hansel, T. L. Hayhurst, D. J. Mabry, M. G. Sivjee, and J. W. Skinner, "LWIR/MWIR imaging hyperspectral sensor for airborne and ground-based remote sensing," in *Proc. SPIE Conf. Imaging Spectrometry II*, vol. 2819, Nov. 1996, pp. 102–107.



**John P. Kerekes** (S'81–M'89–SM'00) received the B.S., M.S., and Ph.D. degrees in electrical engineering from Purdue University, West Lafayette, IN, in 1983, 1986, and 1989, respectively.

From 1983 to 1984, he was a Member of the Technical Staff with the Space and Communications Group, Hughes Aircraft Co., El Segundo, CA, where he performed circuit design for communications satellites. From 1986 to 1989, he was a Graduate Research Assistant, working with both the School of Electrical Engineering and the Laboratory for Applications of Remote Sensing at Purdue University. From 1989 to 2004, he was a Technical Staff Member with the Lincoln Laboratory, Massachusetts Institute of Technology, Lexington. In 2004, he became an Associate Professor in the Center for Imaging Science, Rochester Institute of Technology, Rochester, NY. His research interests include the modeling and analysis of remote sensing system performance in pattern recognition and geophysical parameter retrieval applications.

Dr. Kerekes is a member of Tau Beta Phi, Eta Kappa Nu, the American Geophysical Society, the American Meteorological Society, the American Society for Photogrammetry and Remote Sensing, and SPIE—The International Society for Optical Engineering. From 1995 to 2004, he has served as the Chair of the Boston Section Chapter of the IEEE Geoscience and Remote Sensing Society (GRSS). He has served as the Co-Chair of the GRSS Instrumentation and Future Technology Technical Committee and is the General Co-Chair of IGARSS 2008 to be held in Boston, MA.



**Jerrold E. Baum** received the A.B. degree from Brandeis University, Waltham, MA, in 1975, and the M.S. degree from the University of Maryland, College Park, in 1980, both in physics.

From 1977 to 1985, he taught high school physics in Maryland and Massachusetts. In 1985, he joined Textron Defense Systems, Wilmington, MA, as a Senior Engineer, where he helped develop the detection algorithm for an airborne infrared sensor. Since 1989, he has been an Associate Staff Member with the Lincoln Laboratory, Massachusetts Institute of Technology, Lexington. He is currently involved with modeling and analyzing hyperspectral remote sensing systems. His previous work included analyzing GOES imager satellite data, modeling infrared sensor performance in battlefield simulations, and evaluating active- and passive-infrared detection algorithms.